

Proprioceptive-only State Estimation for Legged Robots with Set-Coverage Measurements of Learned Dynamics

Abhijeet M. Kulkarni¹, Ioannis Poulakakis² and Guoquan Huang¹

Abstract—Proprioceptive-only state estimation is attractive for legged robots since it is computationally cheaper and is unaffected by perceptually degraded conditions. The history of joint-level measurements contains rich information that can be used to infer the dynamics of the system and subsequently produce navigational measurements. Recent approaches produce these estimates with learned measurement models and fuse with IMU data, under a Gaussian noise assumption. However, this assumption can easily break down with limited training data and render the estimates inconsistent and potentially divergent. In this work, we propose a proprioceptive-only state estimation framework for legged robots that characterizes the measurement noise using set-coverage statements that do not assume any distribution. We develop a practical and computationally inexpensive method to use these set-coverage measurements with a Gaussian filter in a systematic way. We validate the approach in both simulation and two real-world quadrupedal datasets. Comparison with the Gaussian baselines shows that our proposed method remains consistent and is not prone to drift under real noise scenarios.

I. INTRODUCTION AND RELATED WORK

Quadrupedal robots have matured into reliable field platforms, demonstrating impressive robustness in challenging, unstructured environments. This capability makes them compelling candidates for missions of subterranean exploration [1], operation in natural environments [2], and industrial inspection [3]. In such domains, accurate state estimation is not merely a supporting module—it is a prerequisite for long-term autonomous operation. While exteroceptive sensors, like LiDAR, cameras, and radar, can provide highly informative measurements for accurate state estimation, they are also the most vulnerable to environmental degradation [4], such as dust, smoke, darkness, specularities, vegetation, and poor texture, leading to intermittent or biased perception and ultimately estimator failure. In contrast, proprioceptive sensing with Inertial Measurement Unit (IMU) and joint-level measurements is unaffected by these perceptually degraded conditions and is routinely relied upon for robust, high-rate control [5]. This motivates *proprioceptive-only* state estimation pipelines that can maintain reliable tracking when exteroception becomes unreliable or unavailable.

Classical proprioceptive state estimation fuses IMU data with leg kinematics using either filtering methods [6], [7] or factor-graph formulations [8], [9]. These approaches can be effective when foot contacts are accurately detected and modeled; however, performance may deteriorate under imperfect

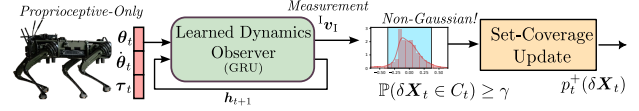


Fig. 1. Proposed method uses *set-coverage* measurements for update.

contact. A key observation is that, during locomotion, the robot’s whole-body motion and contact dynamics under the action of its low-level controller imprint rich structure onto time histories of joint angles, velocities, and torques. This structure has been exploited to extract latent states for learned dynamics models used as predictive components in planning pipelines [10], [11]. Analogously, a *window* of proprioceptive measurements can be exploited to infer body motion. Recent learning-based approaches pursue this direction by training neural networks to extract motion-relevant patterns from proprioceptive histories and produce pseudo-measurements—such as body-frame velocity or relative displacement—that can be fused within a filter [12], [13], [14], [15]. In this view, the network functions as a virtual sensor, whose prediction error is modeled as measurement noise and fused with IMU information in the estimation pipeline.

For computational compatibility with efficient Extended Kalman Filter (EKF) frameworks, these virtual sensors are typically modeled as corrupted by zero-mean Gaussian noise. The corresponding covariances are either fixed [14] or predicted jointly with the mean [12]. In practice, such networks are commonly trained with extensive data and adopt Gaussian Maximum Likelihood (GML) [16] to capture *aleatoric* uncertainty via a predicted covariance. However, collecting large-scale, representative training data is expensive, and simulation-trained models often require careful domain randomization to mitigate sim-to-real mismatch. In the resulting limited-data regime, *epistemic* uncertainty can dominate [17], [18], yielding prediction errors that are biased or non-Gaussian and poorly characterized by the learned aleatoric covariance [19]. When such miscalibrated pseudo-measurements are fused as if they were Gaussian, the filter can become overconfident and may diverge.

A number of estimators relax the Gaussian assumption, but they tend to trade off modeling fidelity against deployability. Robust Kalman filtering variants can attenuate the impact of occasional outliers [20], yet they are less effective under persistent biases or distribution shifts. Set-membership and related bounded-error methods can handle such systematic deviations [21], [22], but they typically return state sets rather than point estimates, and the set representation can grow in complexity over time. Distributionally robust formulations [23] provide another alternative by optimizing against

¹Department of Mechanical Engineering, University of Delaware, Newark, DE, USA {amkulk, ghuang}@udel.edu

²Robotics Institute, Athena Research Center, Marousi, Greece; School of Mechanical Engineering, National Technical University of Athens, Greece; HERON—Center of Excellence in Robotics, Athens, Greece poulakakis@mail.ntua.gr, i.poulakakis@athenarc.gr.

an ambiguity set over noise distributions, but they require specifying that ambiguity set around a nominal likelihood and are often realized via particle filtering, which can be computationally costly. In contrast, onboard state estimation demands a fast, lightweight recursive update that still returns a point estimate while remaining reliable under non-Gaussian pseudo-measurement errors whose likelihood is not known.

This paper addresses the above failure mode by introducing a state estimation framework that replaces the untrue Gaussian noise assumption with a *set-coverage* uncertainty representation for learned legged dynamics (as pseudo-measurements), see Fig. 1. Specifically, we characterize pseudo-measurement error using calibrated sets that provide probabilistic coverage—i.e., with a prescribed probability, the true error lies inside the set. Such statements can be obtained via modern Uncertainty Quantification (UQ) tools [24], including conformal prediction [25] and scenario optimization [26], and are distribution free. We then develop a principled method to incorporate these set-coverage constraints into a recursive filtering pipeline. In particular, the main contributions of this paper include:

- We propose a novel proprioceptive-only state estimation framework that models learned dynamics-based pseudo-measurement uncertainty via calibrated set-coverage statements, without the untrue Gaussian assumption.
- We develop a practical method to efficiently fuse coverage-constrained pseudo-measurements with the state estimate of a recursive filter. Our implementation is shown to be real-time (e.g., 0.07 ms per update on a laptop CPU), suitable for high-rate onboard estimation.
- The proposed approach is validated extensively in Monte-Carlo simulations and on real-world quadruped experiments, showing improved robustness under non-Gaussian error behavior and preventing divergence cases observed with a Gaussian baseline (EKF) and competitive performance with proprioception baseline.

II. BACKGROUND: LEGGED STATE ESTIMATION WITH INVARIANT FILTERING

In this section, we briefly describe the state estimation for legged robots in the Invariant Extended Kalman Filter (IEKF) framework [7], which serves as the basis for our proposed method. Specifically, we seek to continuously estimate the robot’s base frame $\{I\}$ navigation state relative to a global frame $\{G\}$ using IMU and joint-level proprioceptive data. This navigation state typically comprises the orientation ${}^G_1\mathbf{R} \in \text{SO}(3)$, velocity ${}^G\mathbf{v}_I \in \mathbb{R}^3$, and position ${}^G\mathbf{p}_I \in \mathbb{R}^3$.

A. Preliminaries on $\text{SE}_2(3)$

The robot’s navigation state is modeled as an element of the matrix Lie group $\text{SE}_2(3)$. An element $\chi \in \text{SE}_2(3)$ packs the orientation, velocity, and position into a single matrix representation:

$$\chi = \begin{bmatrix} {}^G_1\mathbf{R} & {}^G\mathbf{v}_I & {}^G\mathbf{p}_I \\ \mathbf{0}_{1 \times 3} & 1 & 0 \\ \mathbf{0}_{1 \times 3} & 0 & 1 \end{bmatrix}. \quad (1)$$

The associated Lie algebra is $\mathfrak{se}_2(3)$. The hat operator $(\cdot)^\wedge : \mathbb{R}^9 \rightarrow \mathfrak{se}_2(3)$ maps a vector $\mathbf{v} \in \mathbb{R}^9$ to the Lie algebra, with the inverse mapping provided by the vee operator

$(\cdot)^\vee : \mathfrak{se}_2(3) \rightarrow \mathbb{R}^9$. The matrix exponential map $\exp(\cdot) : \mathfrak{se}_2(3) \rightarrow \text{SE}_2(3)$ maps the algebra to the group. For small perturbations \mathbf{v} , the exponential map admits the first-order approximation:

$$\exp(\mathbf{v}^\wedge) \approx \mathbf{I} + \mathbf{v}^\wedge. \quad (2)$$

A *right-invariant* error between the estimated state $\bar{\chi}$ and the true state χ :

$$\boldsymbol{\eta} \triangleq \bar{\chi} \chi^{-1} \in \text{SE}_2(3). \quad (3)$$

This invariant error is parameterized in the Lie algebra as

$$\boldsymbol{\eta} = \exp(\boldsymbol{\xi}^\wedge), \quad \text{where } \boldsymbol{\xi} \in \mathbb{R}^9 \quad (4)$$

B. State Representation and IMU Propagation

We augment the navigation state with IMU biases $\mathbf{b}_t \in \mathbb{R}^6$:

$$\mathbf{X}_t = (\chi_t, \mathbf{b}_t), \quad \mathbf{b}_t = [\mathbf{b}_a^\top \ \mathbf{b}_g^\top]^\top.$$

Using the standard IMU model with acceleration ${}^I\mathbf{a}$ and angular rate ${}^I\boldsymbol{\omega}$ both in $\{I\}$ the measurement corrupted with bias and Gaussian noises $\mathbf{n}_a, \mathbf{n}_g$:

$${}^I\tilde{\mathbf{a}} = {}^I\mathbf{a} + \mathbf{b}_a + \mathbf{n}_a, \quad {}^I\tilde{\boldsymbol{\omega}} = {}^I\boldsymbol{\omega} + \mathbf{b}_g + \mathbf{n}_g,$$

And the continuous-time IMU kinematics is given by:

$$\begin{aligned} {}^G_1\dot{\mathbf{R}} &= {}^G_1\mathbf{R} [{}^I\tilde{\boldsymbol{\omega}} - \mathbf{b}_g - \mathbf{n}_g]_\times, \\ {}^G\dot{\mathbf{v}}_I &= \mathbf{g}^G + {}^G_1\mathbf{R} ({}^I\tilde{\mathbf{a}} - \mathbf{b}_a - \mathbf{n}_a), \\ {}^G\dot{\mathbf{p}}_I &= {}^G\mathbf{v}_I, \quad \dot{\mathbf{b}}_a = \mathbf{n}_{ba}, \quad \dot{\mathbf{b}}_g = \mathbf{n}_{bg} \end{aligned} \quad (5)$$

We collect the noise as $\mathbf{w}_t = [\mathbf{n}_a^\top \ \mathbf{n}_g^\top \ \mathbf{n}_{ba}^\top \ \mathbf{n}_{bg}^\top]^\top \in \mathbb{R}^{12}$, $\mathbf{w}_t \sim \mathcal{N}(\mathbf{0}, \mathbf{Q})$ and \mathbf{g}^G is the gravity vector.

Define the augmented error state $\delta\mathbf{X}_t = [\boldsymbol{\xi}_t^\top \ \delta\mathbf{b}_t^\top]^\top \in \mathbb{R}^{15}$, where $\boldsymbol{\xi}_t$ parameterizes the right-invariant error in (4) and $\delta\mathbf{b}_t = \bar{\mathbf{b}}_t - \mathbf{b}_t$. We relate the true and estimate with:

$$\mathbf{X}_t = \bar{\mathbf{X}}_t \boxplus \delta\mathbf{X}_t \triangleq (\exp(-\boldsymbol{\xi}_t^\wedge) \bar{\chi}_t, \bar{\mathbf{b}}_t - \delta\mathbf{b}_t), \quad (6)$$

where \boxplus is the compositional operator, see [7], and assume $\delta\mathbf{X}_t \sim \mathcal{N}(\mathbf{0}, \boldsymbol{\Sigma}_t)$, i.e.,

$$\mathbf{X}_t \sim \bar{\mathbf{X}}_t \boxplus \mathcal{N}(\mathbf{0}, \boldsymbol{\Sigma}_t). \quad (7)$$

Linearizing the error dynamics yields

$$\frac{d}{dt} \delta\mathbf{X}_t = \mathbf{A}_t \delta\mathbf{X}_t + \mathbf{N}_t \mathbf{w}_t, \quad (8)$$

with \mathbf{A}_t and \mathbf{N}_t as in [7]. Over Δt , the mean is propagated by integrating the nominal dynamics (5) with zero noise and the covariance is propagated as:

$$\boldsymbol{\Sigma}_{t+\Delta t} = \boldsymbol{\Phi} \boldsymbol{\Sigma}_t \boldsymbol{\Phi}^\top + \mathbf{Q}_d. \quad (9)$$

where $\boldsymbol{\Phi} = \exp(\mathbf{A}_t \Delta t)$ and $\mathbf{Q}_d \approx \boldsymbol{\Phi} \mathbf{N}_t \mathbf{Q} \mathbf{N}_t^\top \boldsymbol{\Phi}^\top \Delta t$.

C. Invariant Measurement Output

Following the invariant observer design, we define a right-invariant output \mathbf{y}_t with a known constant vector \mathbf{d} :

$$\begin{aligned} \mathbf{y}_t &= \chi_t^{-1} \mathbf{d}, \\ &= \begin{bmatrix} ({}^G_1\mathbf{R})^\top & -{}^G_1\mathbf{R}^\top {}^G\mathbf{v}_I - {}^G_1\mathbf{R}^\top {}^G\mathbf{p}_I \\ \mathbf{0} & 1 \\ \mathbf{0} & 0 \end{bmatrix} \begin{bmatrix} \mathbf{0}_{3 \times 1} \\ -1 \\ 0 \end{bmatrix} = \begin{bmatrix} {}^I\mathbf{v}_I \\ -1 \\ 0 \end{bmatrix}. \end{aligned} \quad (10)$$

where ${}^G_1\mathbf{R}^\top {}^G\mathbf{v}_I = {}^I\mathbf{v}_I$ is the body-frame velocity, and the last two components are constants of the homogeneous structure of the invariant output. The measurements are assumed to be corrupted by an additive noise $\boldsymbol{\nu}_t$ such that the complete measurement model is

$$\mathbf{y}_t = \chi_t^{-1} \mathbf{d} + \boldsymbol{\nu}_t \quad (11)$$

In the next, we discuss our approach to obtain the body-frame velocity ${}^I\mathbf{v}_I$ and characterization of the noise $\boldsymbol{\nu}_t$.

III. MODELING LEARNED LEGGED DYNAMICS

Proprioceptive signals do not directly measure navigational quantities such as the body-frame velocity ${}^I\mathbf{v}_I$. However, legged locomotion induces strong dynamical couplings between joint kinematics/torques, and base motion. These couplings can be exploited to observe the system's latent state \mathbf{h} , allowing for the construction of pseudo-measurements of ${}^I\mathbf{v}_I$ from short histories of proprioceptive data. In section, we learn a dynamical observer to generate these pseudo-measurements and address how to represent their prediction uncertainty for robust recursive estimation.

A. Proprioceptive Observation Model

A typical quadrupedal robot features 12 joints across its four legs, with three joints per leg (two at the hip and one at the knee). Accordingly, the joint-level proprioceptive observation at time t is defined as $\mathbf{o}_t := (\boldsymbol{\theta}_t, \dot{\boldsymbol{\theta}}_t, \boldsymbol{\tau}_t) \in \mathbb{T}^{12} \times \mathbb{R}^{12} \times \mathbb{R}^{12}$, representing joint angles, velocities, and torques, respectively. Motivated by prior efforts on learning dynamical observers from short proprioceptive windows [10], [11], we feed a finite proprioceptive history to a learned observer that also outputs an instantaneous pseudo-measurement of the body-frame velocity.

To model this observer, after evaluating a set of popular lightweight architectures (including MLP, RNN, LSTM, Bi-GRU, and TCN) on our limited training data, we employ a Gated Recurrent Unit (GRU) network as it achieved the best performance. Let ϕ_ψ denote the learned dynamical observer with parameters ψ and latent state $\mathbf{h}_t \in \mathbb{R}^h$. The observer updates its latent state and outputs a pseudo-measurement of the body-frame velocity ${}^I\tilde{\mathbf{v}}_{I_t} \in \mathbb{R}^3$ as follows:

$$(\mathbf{h}_t, {}^I\tilde{\mathbf{v}}_{I_t}) = \phi_\psi(\mathbf{o}_t, \mathbf{h}_{t-\Delta t}) \quad (12)$$

The prediction error is given by:

$$\mathbf{e}_t = {}^I\tilde{\mathbf{v}}_{I_t} - {}^I\mathbf{v}_{I_t} \Rightarrow \boldsymbol{\nu}_t = \tilde{\mathbf{y}}_t - \mathbf{y}_t = \begin{bmatrix} \mathbf{e}_t \\ 0 \\ 0 \end{bmatrix}, \quad (13)$$

which is also treated as the measurement noise in the right-invariant output (11).

B. Supervised Training

We train the dynamics observer network ϕ_ψ using supervised trajectories with ground-truth body-frame velocities:

$$\mathcal{D}_{\text{train}} = \left\{ \left\{ (\mathbf{o}_{k\Delta t}^{(i)}, {}^I\mathbf{v}_{I_{k\Delta t}}^{(i)}) \right\}_{k=0}^T \right\}_{i=1}^{N_{\text{train}}}, \quad (14)$$

where i indexes trajectories, each of length T , and ${}^I\mathbf{v}_{I_{k\Delta t}}^{(i)}$ is obtained from motion capture or a high-accuracy reference estimator. The observer latent state is set to zero at the start of each trajectory, $\mathbf{h}_0 = \mathbf{0}$, and parameters ψ can be learned with MSE loss or GML loss [16], that can predict covariances. We use a single GRU layer, with hidden size $h = 64$, train on sequences of length $T = 1000$ at $\Delta t = 10$ ms, with the following two datasets:¹

¹Note that we here intended to choose a small network primarily to avoid overfitting to the limited data.

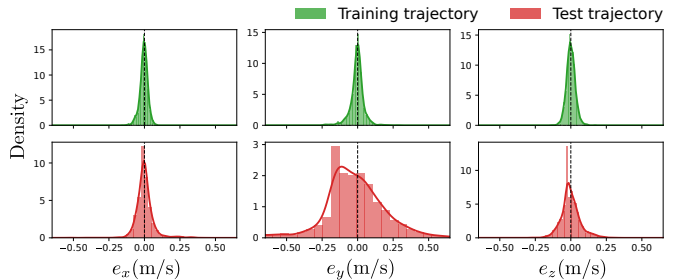


Fig. 2. Prediction error \mathbf{e}_t of the learned velocity predictor for Vision60 on the training trajectory (green) versus a test trajectory (red).

1) *Vision60 dataset*: This is our own dataset and the ground truth is provided by a motion-capture system. From the available sequences (Tab. IV), we train on a single trajectory to keep the supervised training protocol controlled while ensuring coverage of common locomotion regimes. Specifically, we use 3CC3CCW, which contains repeated segments of straight walking as well as left and right turning (clockwise and counterclockwise loops), and thus exposes the observer to typical gait transitions within one continuous run. The sequence lasts 108 s and is ≈ 75 m long.

2) *Spot dataset*: This dataset [9] has the ground-truth velocity provided by a high-precision perception-based reference estimator. To mirror the Vision60 setup, we likewise train on a single representative sequence and use the remaining data for evaluation. Concretely, we train on the UPSTAIR sequence, which includes sustained locomotion with direction changes under the provided reference estimates.

C. Gaussianity Fails From Training to Testing

A standard modeling assumption in learned-measurement pipelines is to treat the prediction error as a zero-mean Gaussian process: $\mathbf{e}_t \sim \mathcal{N}(\mathbf{0}, \mathbf{R}_t)$, which facilitates fusion with IMU data via EKF. This approximation is often valid when the error distribution is unbiased and unimodal, to achieve this performance typically a large, representative training datasets is required. As shown in Fig. 2, the Vision60 network's error on the training data closely approximates a Gaussian distribution, where aleatoric uncertainty can be effectively captured by GML-based covariance prediction.

However, in realistic field deployments where training data is limited, epistemic uncertainty becomes dominant when the model encounters out-of-training distribution data [17], [18]. In such cases, the induced error may exhibit varying multi-modality, skewness, or heavy tails—characteristics not captured by a fixed parametric noise model. Fig. 2 illustrates this phenomenon: when the network trained on a single sequence (Section III-B.1) is evaluated on a test trajectory, the prediction errors *deviate significantly from Gaussianity*, especially in the forward y -direction of motion.

D. Error-State Coverage Statements

To overcome the above limitations of Gaussian noise models, we characterize the learned predictor errors using *set-coverage statements* [27, Section 9.3.2], which constrain only the *probability mass* assigned to a calibrated set and are therefore agnostic to the unknown (or hard-to-model)

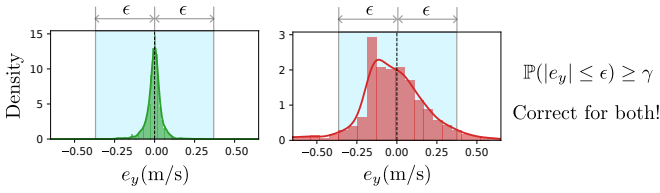


Fig. 3. A single calibrated coverage statement can remain valid for both training (green) and test (red) error distributions.

true *probability distribution* of the errors. Concretely, for the velocity prediction error e_t , we assume the following bound $\epsilon \in \mathbb{R}_{\geq 0}^3$ such that

$$\mathbb{P}(|e_t| \leq \epsilon) \geq \gamma, \quad (15)$$

where $|\cdot|$ denotes element-wise absolute value and $\gamma \in (0, 1)$ is the desired confidence level (probability). Fig. 3 illustrates an example with $\gamma = 0.85$, where the same coverage set remains compatible with both in-distribution (training) and shifted (test) errors.

Note that the coverage bounds (15) can be obtained using distribution-free UQ procedures such as conformal prediction [28] or scenario-optimization-based calibration [26]. Because these coverage statements can be computed *post-hoc*, they apply to any frozen predictor [28] and avoid costly retraining when the deployment environment shifts, while capturing both aleatoric and epistemic uncertainty [29]. If the training data poorly represent calibration/deployment conditions, the resulting ϵ may become conservative. We will detail the specific calibration procedure used in our experiments in Section VI-A.

Remark 1. A coverage statement is weaker than explicit likelihood. It constrains only the probability mass assigned to a set and leaves the distribution inside and outside that set unspecified. This makes the framework flexible enough to accommodate non-Gaussian, multimodal, and heavy-tailed errors distributions. This is a core advantage and enables the use of coverage guarantees without requiring restrictive modeling assumptions on the measurement noise.

To the best of our knowledge, we are the *first* to utilize this flexible set-coverage statement (15) to model learned legged dynamics, rather than using an ad-hoc Gaussian model. Specifically, we express the calibrated velocity-error coverage statement directly in the augmented error state $\delta \mathbf{X}_t$ (6). Using the measurement model (11) together with $\boldsymbol{\nu}_t = [e_t^\top \ 0 \ 0]^\top$. We define the projection $\Pi := [I_{3 \times 3} \ \mathbf{0}_{3 \times 2}]$, so that the coverage set $|e_t| \leq \epsilon$ is equivalently

$$|\Pi(\boldsymbol{\chi}_t^{-1} \mathbf{d} - \tilde{\mathbf{y}}_t)| \leq \epsilon. \quad (16)$$

With the right-invariant error (3), substituting $\boldsymbol{\chi}_t^{-1} = \bar{\boldsymbol{\chi}}_t^{-1} \boldsymbol{\eta}_t$ in above and using first-order approximation (2), we have

$$\Pi(\boldsymbol{\chi}_t^{-1} \mathbf{d} - \tilde{\mathbf{y}}_t) \approx \Pi(\bar{\boldsymbol{\chi}}_t^{-1} \mathbf{d} - \tilde{\mathbf{y}}_t) + \mathbf{H} \delta \mathbf{X}_t, \quad (17)$$

where $\mathbf{H} \in \mathbb{R}^{3 \times 15}$ is the linear map $\mathbf{H} \delta \mathbf{X}_t = \Pi \bar{\boldsymbol{\chi}}_t^{-1} \boldsymbol{\xi}_t^\wedge \mathbf{d}$ (the bias components do not enter). Hence the coverage constraint induces the error-state feasible set:

$$C_t = \{\delta \mathbf{X}_t \in \mathbb{R}^{15} : \mathbf{l}_t \leq \mathbf{H} \delta \mathbf{X}_t \leq \mathbf{u}_t\} \quad (18)$$

$$\mathbf{l}_t = -\Pi(\bar{\boldsymbol{\chi}}_t^{-1} \mathbf{d} - \tilde{\mathbf{y}}_t) - \epsilon \quad (19)$$

$$\mathbf{u}_t = -\Pi(\bar{\boldsymbol{\chi}}_t^{-1} \mathbf{d} - \tilde{\mathbf{y}}_t) + \epsilon \quad (20)$$

Clearly, (15) is equivalent to the error-state coverage statement (see [27, Thm. 9.2.2]):

$$\mathbb{P}(\delta \mathbf{X}_t \in C_t) \geq \gamma. \quad (21)$$

In the next, we will discuss how the error-state coverage statement is used to update the current state estimate. Once the posterior $\delta \mathbf{X}_t^+ \sim \mathcal{N}(\boldsymbol{\mu}_t^+, \mathbf{P}_t^+)$ satisfying (21) is obtained, the on-manifold update is $\mathbf{X}_t^+ = \bar{\mathbf{X}}_t \boxplus \delta \mathbf{X}_t^+$.

IV. OUR PROPRIOCEPTIVE-ONLY STATE ESTIMATOR

In this section, we present how to rigorously incorporate the set-coverage statement (21) into our proposed proprioceptive-only state estimator in the IEKF framework. As the IMU propagation is standard as in Section II-B, in the following we focus on the coverage measurement update and its practical efficient implementation.

A. Coverage-Constrained Update

After the IEKF propagation with IMU (see Section II-B), we have the following prior Gaussian estimate at time t :

$$\bar{p}_t(\delta \mathbf{X}) := \mathcal{N}(\delta \mathbf{X}; \bar{\boldsymbol{\mu}}_t, \bar{\boldsymbol{\Sigma}}_t), \quad (22)$$

with $\bar{\boldsymbol{\mu}}_t = \mathbf{0}$ (kept for the generality). We seek to find the posterior distribution $p^+(\delta \mathbf{X})$ that: (i) assigns at least γ probability mass to C_t , and (ii) deviates minimally from \bar{p}_t in Kullback-Leibler (KL) divergence, as in minimum cross-entropy [30] and posterior regularization [31] approaches:

$$p_t^* := \arg \min_p \text{KL}(p \| \bar{p}_t) \quad (23)$$

$$\begin{aligned} \text{s.t.} \quad & \int_{C_t} p(\delta \mathbf{X}) \, d(\delta \mathbf{X}) \geq \gamma, \\ & \int p(\delta \mathbf{X}) \, d(\delta \mathbf{X}) = 1, \quad p(\delta \mathbf{X}) \geq 0 \end{aligned}$$

Note that the objective $\text{KL}(p \| \bar{p}_t)$ is strictly convex in p , and the constraints are linear in p , hence (23) is a convex optimization problem [31] and assumes a unique minimizer. The following result shows that enforcing the coverage constraint admits a closed-form update solution:

Theorem 1 (KL-minimal posterior with a set-mass constraint). *Assume $\bar{p}_t(\delta \mathbf{X}) > 0$ almost everywhere on its support. Let C_t be measurable, $\gamma \in (0, 1)$, and let*

$$\pi_t := \int_{C_t} \bar{p}_t(\delta \mathbf{X}) \, d(\delta \mathbf{X}). \quad (24)$$

If $\pi_t \geq \gamma$, then the unique minimizer of (23) is $p_t^ = \bar{p}_t$. If $\pi_t < \gamma$ and $0 < \pi_t < 1$, then the unique minimizer is*

$$p_t^* = \frac{\gamma}{\pi_t} \bar{p}_t \mathbf{1}_{C_t}(\delta \mathbf{X}) + \frac{1-\gamma}{1-\pi_t} \bar{p}_t \mathbf{1}_{(C_t)^c}(\delta \mathbf{X}). \quad (25)$$

Proof. See Appendix I. \square

This result implies a simple update rule. If the prior already meets the coverage requirement ($\pi_t \geq \gamma$), the constraint is inactive and no modification is required: $p_t^+ = \bar{p}_t$, hence $\boldsymbol{\mu}_t^+ = \bar{\boldsymbol{\mu}}_t$ and $\boldsymbol{\Sigma}_t^+ = \bar{\boldsymbol{\Sigma}}_t$. If instead $\pi_t < \gamma$, the KL-minimal projection rescales the prior inside and outside C_t so that $\mathbb{P}_{p_t^*}(\delta \mathbf{X} \in C_t) = \gamma$. Since the resulting p_t^* is

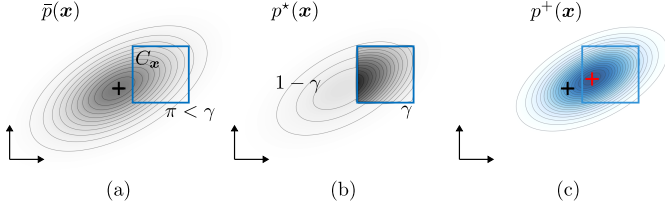


Fig. 4. Illustration of the KL-minimal belief update with a coverage constraint. (a) Prior with $\pi_t < \gamma$. (b) Exact KL-optimal posterior: piecewise rescaling of the prior inside/outside C_t . (c) Gaussian approximation obtained by moment matching.

generally non-Gaussian, we restore a Gaussian representation by moment matching for recursive Gaussian estimation.²

B. Gaussian Moment Matching

Our goal is to construct a Gaussian posterior p_t^+ whose first two moments match those of the optimal posterior p_t^* . To this end, define the prior second moment as $M_t := \bar{\Sigma}_t + \bar{\mu}_t \bar{\mu}_t^\top$. Then the truncated moments of the prior on C_t are:

$$\begin{aligned} \mu_{C_t} &:= \frac{1}{\pi_t} \int_{C_t} \delta \mathbf{X} \bar{p}_t(\delta \mathbf{X}) d(\delta \mathbf{X}), \\ M_{C_t} &:= \frac{1}{\pi_t} \int_{C_t} \delta \mathbf{X} \delta \mathbf{X}^\top \bar{p}_t(\delta \mathbf{X}) d(\delta \mathbf{X}). \end{aligned} \quad (26)$$

The corresponding moments on the complement follow from the law of total expectation:

$$\mu_{C_t^c} = \frac{\bar{\mu}_t - \pi_t \mu_{C_t}}{1 - \pi_t}, \quad M_{C_t^c} = \frac{M_t - \pi_t M_{C_t}}{1 - \pi_t}. \quad (27)$$

Finally, the moment-matched Gaussian posterior $p_t^+(\delta \mathbf{X}) = \mathcal{N}(\delta \mathbf{X}; \mu_t^+, \Sigma_t^+)$ is obtained as

$$\mu_t^+ = \gamma \mu_{C_t} + (1 - \gamma) \mu_{C_t^c}, \quad (28)$$

$$M_t^+ = \gamma M_{C_t} + (1 - \gamma) M_{C_t^c}, \quad (29)$$

$$\Sigma_t^+ = M_t^+ - \mu_t^+ (\mu_t^+)^{\top}. \quad (30)$$

Fig. 4 illustrates the update process from obtaining optimal posterior to its moment-matched Gaussian. The main computational cost is evaluating π_t in (24) and the truncated moments in (26), which require integrating a multivariate Gaussian over the set C_t in \mathbb{R}^{15} (see (18)). Next we exploit the structure of C_t to reduce the integration dimension and then use numerical methods [32] to compute these integrals.

C. Reduced-Dimensional Implementation

Note that for (18), the constraint depends on $\delta \mathbf{X}_t$ only through $\mathbf{z}_t := \mathbf{H} \delta \mathbf{X}_t \in \mathbb{R}^3$, with component-wise bounds $\mathbf{l}_t \leq \mathbf{z}_t \leq \mathbf{u}_t$. Thus we can perform the expensive probability and truncated-moment computations in the output space \mathbb{R}^3 . Under the Gaussian prior $\delta \mathbf{X}_t \sim \mathcal{N}(\bar{\mu}_t, \bar{\Sigma}_t)$, the projected prior on \mathbf{z}_t is given by:

$$\mathbf{z}_t \sim \mathcal{N}(\bar{\mu}_{z,t}, \bar{\Sigma}_{z,t}) = \mathcal{N}(\mathbf{H} \bar{\mu}_t, \mathbf{H} \bar{\Sigma}_t \mathbf{H}^\top). \quad (31)$$

The coverage set becomes an axis-aligned box:

$$C_t^z := \{\mathbf{z} \in \mathbb{R}^3 \mid \mathbf{l}_t \leq \mathbf{z} \leq \mathbf{u}_t\}. \quad (32)$$

²Moment matching is equivalent to reverse-direction KL minimization $q^* = \arg \min_{q \in \mathcal{G}} \text{KL}(q \| p_t^*)$, where \mathcal{G} is the family of Gaussians.

Algorithm 1 Coverage-Constrained Measurement Update

Require: Prior state $\bar{\mathbf{X}}_t$, prior error moments $(\bar{\mu}_t, \bar{\Sigma}_t)$, pseudo-measurement $\tilde{\mathbf{y}}_t$, bounds ϵ , confidence γ

Ensure: Updated state \mathbf{X}_t^+ , updated error covariance Σ_t^+

- 1: Form $\mathbf{l}_t, \mathbf{u}_t, \mathbf{H}$, and C_t via (18).
 - 2: Project prior to constraint space using (31).
 - 3: Compute $\pi_t = \mathbb{P}(\mathbf{z}_t \in C_t^z)$ and truncated moments in \mathbf{z} -space with [32].
 - 4: **if** $\pi_t \geq \gamma$ **then**
 - 5: $\mu_t^+ \leftarrow \bar{\mu}_t, \Sigma_t^+ \leftarrow \bar{\Sigma}_t, \mathbf{X}_t^+ \leftarrow \bar{\mathbf{X}}_t$
 - 6: **return** $\mathbf{X}_t^+, \Sigma_t^+$
 - 7: **end if**
 - 8: Moment match in \mathbf{z} -space to obtain $(\mu_{z,t}^+, \Sigma_{z,t}^+)$ via (28).
 - 9: Lift to full space using (33)–(34) to get (μ_t^+, Σ_t^+) .
 - 10: On-manifold update: $\mathbf{X}_t^+ \leftarrow \bar{\mathbf{X}}_t \boxplus \mu_t^+$.
 - 11: **return** $\mathbf{X}_t^+, \Sigma_t^+$
-

We apply Theorem 1 and the moment-matching update (28) directly in \mathbf{z} -space to obtain an updated marginal $\mathbf{z}_t \sim \mathcal{N}(\mu_{z,t}^+, \Sigma_{z,t}^+)$, where $\pi_t = \mathbb{P}(\mathbf{z}_t \in C_t^z)$ on the prior.

To recover a Gaussian distribution over $\delta \mathbf{X}_t \in \mathbb{R}^{15}$, we keep the *prior conditional* $p(\delta \mathbf{X}_t \mid \mathbf{z}_t)$ and replace only the marginal over \mathbf{z}_t . This preserves the prior cross-correlations between constrained and unconstrained components while updating uncertainty only in the directions informed by the coverage constraint. Then the lifted Gaussian posterior has moments:

$$\mu_t^+ = \bar{\mu}_t + \mathbf{K}_t (\mu_{z,t}^+ - \bar{\mu}_{z,t}), \quad (33)$$

$$\Sigma_t^+ = \bar{\Sigma}_t + \mathbf{K}_t (\Sigma_{z,t}^+ - \mathbf{S}_t) \mathbf{K}_t^\top. \quad (34)$$

where $\mathbf{S}_t = \mathbf{H} \bar{\Sigma}_t \mathbf{H}^\top$ and $\mathbf{K}_t = \bar{\Sigma}_t \mathbf{H}^\top \mathbf{S}_t^{-1}$. Algorithm 1 summarizes the main steps of this implementation.

Remark 2. Equation (34) admits a useful interpretation. If $\Sigma_{z,t}^+ = \mathbf{0}$, then (34) reduces to the standard Kalman covariance update corresponding to an exact (noise-free) observation of \mathbf{z}_t . For $\Sigma_{z,t}^+ \geq \mathbf{0}$, the term $\mathbf{K}_t \Sigma_{z,t}^+ \mathbf{K}_t^\top$ re-injects residual uncertainty along the output directions, reflecting that the set-coverage statement specifies a set-probability condition rather than a noise-free measurement.

V. MONTE-CARLO SIMULATIONS

We validate the proposed set-coverage measurement update in Monte Carlo simulations. The objectives are to: (i) characterize the runtime–accuracy trade-off of estimating the truncated probability mass and moments required by the update, and (ii) compare filter behavior against a standard IEKF [7] correction under both correctly specified Gaussian noise and deliberately misspecified non-Gaussian noise.

Theorem 1 and the moment matching in (28) require prior inset probability mass (24) π_t and truncated moments (26) under the prior $\mathbf{z}_t \sim \mathcal{N}(\bar{\mu}_{z,t}, \bar{\Sigma}_{z,t})$. We approximate these integrals with a randomized (quasi-)Monte Carlo estimator for Gaussian box probabilities and moments (cf. [32]). We compare accuracy with absolute error in π_t , ℓ_2 error of the truncated mean, and Frobenius norm of the truncated covariance, each relative to a 10^7 -sample reference. Tab. I shows the resulting runtime–accuracy trade-off on a Laptop

TABLE I

RUNTIME-ACCURACY FOR TRUNCATED-MOMENT COMPUTATIONS.				
Samples	Timing (ms)	Prob. Error	Mean Error	Cov. Error
100	0.0125	3.12e-4	1.03e-1	2.32e-1
500	0.0372	8.07e-5	2.10e-2	6.72e-2
1000	0.0664	2.00e-5	1.48e-2	3.14e-2
5000	0.302	5.33e-6	3.46e-3	6.46e-3
10000	0.532	1.06e-6	2.06e-3	3.20e-3
(Ref.) 1e7	818.23	0	0	0

i9-13950HX CPU. We use $N = 1000$ samples in all subsequent experiments, which yields sub-millisecond cost (≈ 0.07 ms/update) with sufficiently small errors.

To set up the comparison, we simulate a rigid body following a quadrupedal base-motion trajectory and generate ideal IMU and body-frame velocity outputs consistent with (5)–(11). IMU signals are corrupted with known fixed biases and additive white noise. The body-frame velocity pseudo-measurement is corrupted by an additive error process e_t .

We compare a standard IEKF correction that assumes e_t is zero-mean Gaussian with covariance \mathbf{R} , against the proposed set-coverage update in z -space (Section IV-C). The set-coverage update uses $N = 1000$ samples to estimate π_t and truncated moments, followed by the lift to the error-state space. For this update, the bounds $(\mathbf{I}_t, \mathbf{u}_t)$ are formed from the calibrated elementwise radius ϵ as in (18), set from the γ -quantiles of the noise used to generate measurements.

We evaluate these methods under two specific noise regimes. In the unbiased Gaussian regime, $e_t \sim \mathcal{N}(\mathbf{0}, \mathbf{R}_*)$ and the IEKF uses $\mathbf{R} = \mathbf{R}_*$. This isolates the performance cost of replacing a full likelihood with a weaker set-coverage statement (Remark 1). In the misspecified non-Gaussian regime, we generate e_t from a Gaussian mixture with nonzero component means. For each Monte Carlo trial, we draw one mixture component and keep it fixed over the entire trajectory. The IEKF uses a single Gaussian covariance \mathbf{R} fitted to the mixture, while the coverage bounds are set from outer quantiles. This produces persistent, trial-dependent bias relative to the IEKF’s assumed zero-mean Gaussian model.

Tab. II reports position RMSE and position NEES ($\text{NEES}_{\text{pos}} = 3$ for 3D position, ideally). In the well-specified Gaussian regime, the IEKF achieves the best accuracy and near-nominal consistency, whereas the set-coverage update has higher RMSE because it only exploits mass in the set rather than the full Gaussian shape. However, in the misspecified regime, the IEKF becomes severely inconsistent with a large NEES due to overconfident corrections under an incorrect likelihood model. In contrast, the set-coverage update maintains near-nominal consistency across γ while remaining competitive in RMSE. Operationally, this benefit comes from re-injecting uncertainty along the constrained directions (Remark 2). Ultimately, the set-coverage update is most valuable when pseudo-measurement errors are misspecified, such as being non-Gaussian or biased over a trajectory, where it improves consistency by mitigating overconfident corrections.

Remark 3. *The moment-matched Gaussian approximation does not, in general, preserve the exact set-mass constraint, so the post-approximation probability mass in the feasible set*

TABLE II

UNBIASED/BIASED NOISE MONTE CARLO COMPARISON.				
γ	RMSE (m) (unbiased/biased)		NEES _{pos} (unbiased/biased)	
	EKF update			
–	0.6133 \pm 0.2546 / 2.3298 \pm 1.4016		3.1139 \pm 2.5023 / 99.8873 \pm 121.1403	
	Set-coverage update			
0.70	0.9063 \pm 0.3111 / 2.9453 \pm 1.0126		2.5220 \pm 1.1528 / 1.8621 \pm 1.3769	
0.75	0.8500 \pm 0.2590 / 2.8397 \pm 1.2102		3.5934 \pm 2.4633 / 3.0924 \pm 3.6713	
0.80	0.9402 \pm 0.2702 / 2.6030 \pm 1.3559		4.8568 \pm 2.4530 / 1.9772 \pm 2.6391	
0.85	0.8600 \pm 0.3257 / 3.0532 \pm 1.3384		4.4314 \pm 4.3258 / 3.7381 \pm 5.5225	
0.90	0.9450 \pm 0.2910 / 2.6683 \pm 1.1898		4.6952 \pm 2.8569 / 4.0185 \pm 5.2741	
0.95	1.0468 \pm 0.3559 / 3.3612 \pm 1.4733		3.8479 \pm 2.4304 / 3.7676 \pm 4.6494	

need not equal γ . Empirically, we observe that the update reliably increases the feasible-set mass toward the target (typically $\pi_t < \pi_t^+ \leq \gamma$). While one could iterate the projection/moment-matching to approach γ more tightly, we find that at high update rates a single update per timestep is sufficient in practice. A formal analysis of this behavior is left for the future work.

VI. REAL-WORLD EXPERIMENTS

We further evaluate the proposed set-coverage update on two real-world quadruped datasets (Vision60 and Spot) using the learned pseudo-measurement model (see Section III). We compare our approach against two baselines: (i) a contact-aided leg kinematics-based IEKF [7], and (ii) a learned pseudo-measurement model that outputs mean and covariance [16] with IEKF update [14]. Additionally, for the Spot dataset we compare against a *perceptive* radar-based odometry baseline GaRLILEO [9].

A. Calibration and Coverage Statements

To quantify uncertainty in the pseudo-measurements, we utilize a separate calibration dataset $\mathcal{E}_{\text{cal}} = \{e_{t_k}\}_{k=0}^{T_{\text{Seq}}}$ of measurement errors from the trained network ϕ_ψ . Since the data-generating process is a dynamical system, samples are temporally dependent. To address this complication in practice, we assume the error process is β -mixing [33]:

Assumption 1 (β -mixing). *The error process $\{e_t\}_{t \geq 0}$ is stationary and β -mixing with coefficient $\beta(k) \rightarrow 0$ as $k \rightarrow \infty$.*

Assumption 1 allows for approximately independent calibration samples by subsampling at intervals of K [33]. This yields the subsampled set $\mathcal{E}_{\text{cal}}^{\text{Sub}} = \{e_{t_i}\}_{i=0}^{N_{\text{cal}}}$, where $t_i = iK\Delta t$ and $N_{\text{cal}} = T_{\text{Seq}}/K$. We apply split-conformal prediction [28], [25] using the absolute error in each direction as the score function: $s_{j,i} = |e_{j,t_i}|$ for $j \in \{x, y, z\}$. To obtain a joint confidence level γ for the 3D error vector, we target the per-axis confidence $\tilde{\gamma} = \gamma^{1/3}$, and set the corresponding significance level $\tilde{\alpha} = 1 - \tilde{\gamma}$. Using the standard finite-sample correction, we compute the conformal quantile level based on $k = [(N_{\text{cal}} + 1)(1 - \tilde{\alpha})]$ [28], [25], yielding thresholds $\epsilon = [\epsilon_x, \epsilon_y, \epsilon_z]^\top$ such that $\mathbb{P}(|e_{j,t}| \leq \epsilon_j) \geq \tilde{\gamma}$ for each j . Assuming independence across coordinates, this implies the joint coverage $\mathbb{P}(|e_t| \leq \epsilon) = \prod_{j \in \{x, y, z\}} \mathbb{P}(|e_{j,t}| \leq \epsilon_j) \geq \tilde{\gamma}^3 = \gamma$. The resulting constraints on e_t define the feasible set C_t (18) for the coverage-constrained update.

B. Estimation Performance

Both real-world datasets pose distinct challenges. Vision60 is recorded in a motion-capture room at 100 Hz using on-board IMU and joint measurements. The trajectories are

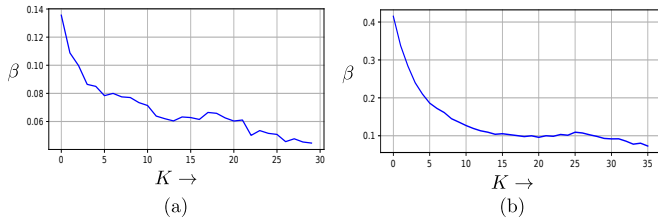


Fig. 5. β -mixing coefficients for Vision60 (a) and Spot (b) calibration data.

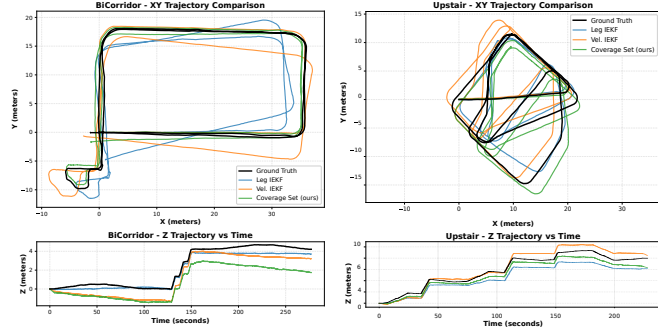


Fig. 6. Two of the representative trajectories of the Spot dataset and with comparison with the baselines.

short and confined to a single room, but include sharp turns and walking over slippery sheets. In contrast, the Spot dataset [9] covers diverse indoor and outdoor terrain with elevation changes. Sequences last multiple minutes and span hundreds of meters, which is particularly challenging for proprioceptive-only odometry.

We set the target coverage level to $\gamma = 0.8$, as we did not observe significant performance difference for $\gamma \in [0.7, 0.85]$ (see Tab. II). From the β -mixing decay in Fig. 5, we choose subsampling intervals $K = 20$ for Vision60 and $K = 35$ for Spot to approximately satisfy the conformal independence requirement with $\beta \approx 0.05$. This yields calibrated coverage bounds $\epsilon = [0.05, 0.2, 0.05]^T$ on Vision60 using the ROOMSCAN sequence and $\epsilon = [0.22, 0.05, 0.1]^T$ on Spot using the QUAD sequence.

Tables IV and III report the absolute and relative RMSE for both datasets. Overall, the proposed set-coverage

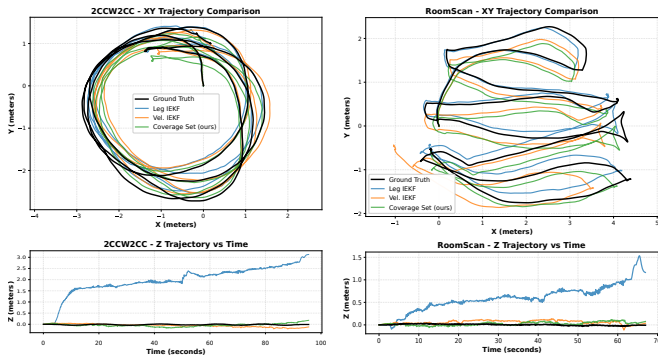


Fig. 7. Two of the representative trajectories of the Vision60 dataset and with comparison with the baselines.

update remains robust and accurate. On Spot dataset, proprioception-only baselines accumulate substantial drift during sharp turns and abrupt elevation changes, especially in DOWNSTAIR and OVERPASS. In these cases, our estimator remains accurate and stable. See Fig. 6 for representative trajectories. Relative to the *perception-based* GaRLILEO, our *proprioception-only* method achieves similar accuracy and even exceeds it on QUAD sequence; GaRLILEO results are taken from [9]. Similarly, on the Vision60, the standard Leg IEKF exhibits significant vertical drift and high position RMSE (Fig. 7). While learned pseudo-measurements can correct this on flat ground, our method yields the lowest absolute position errors overall amongst the baselines. Overall, by effectively handling non-Gaussian noise, our approach outperforms existing proprioceptive methods while maintaining competitiveness with perception-driven baselines.

TABLE III
RESULTS ON SPOT DATASET

Sequence	Method	APE _{trans} [m]	RPE _{trans} [m]	APE _{rot} [deg]	RPE _{rot} [deg/m]	$\pi < \gamma$ [%]
Atrium 109.93 m 124.50 s	GaRLILEO	0.816	0.055	1.715	0.554	–
	Leg IEKF	2.267	0.108	6.457	0.908	–
	Vel. IEKF	0.453	0.037	2.566	1.494	–
	Ours	1.094	0.055	2.075	1.746	69.7
BiCorridor 240.82 m 277.29 s	GaRLILEO	1.425	0.063	5.519	0.885	–
	Leg IEKF	3.251	0.141	9.130	1.413	–
	Vel. IEKF	2.236	0.110	4.118	2.436	–
	Ours	2.526	0.074	2.658	1.955	70.0
BridgeLoop 161.17 m 187.20 s	GaRLILEO	1.193	0.080	2.719	1.058	–
	Leg IEKF	1.235	0.176	6.479	3.439	–
	Vel. IEKF	3.782	0.151	5.027	2.742	–
	Ours	1.421	0.075	2.228	2.307	73.3
CorriLoop 208.68 m 229.40 s	GaRLILEO	1.627	0.066	5.676	0.738	–
	Leg IEKF	3.302	0.116	10.838	1.133	–
	Vel. IEKF	1.198	0.082	4.402	1.986	–
	Ours	2.223	0.068	4.170	2.280	74.0
Downstair 233.75 m 270.90 s	GaRLILEO	3.916	0.099	3.415	1.080	–
	Leg IEKF	8.658	0.135	9.919	1.261	–
	Vel. IEKF	45.689	0.875	3.526	2.639	–
	Ours	6.832	0.106	9.541	2.089	70.2
Overpass 169.17 m 213.49 s	GaRLILEO	1.526	0.091	4.043	1.227	–
	Leg IEKF	43.267	1.522	27.234	5.870	–
	Vel. IEKF	40.923	0.846	4.870	3.367	–
	Ours	2.897	0.054	4.866	1.763	70.6
Quad 447.83 m 503.69 s	GaRLILEO	7.347	0.080	3.356	0.838	–
	Leg IEKF	27.624	0.111	22.735	0.902	–
	Vel. IEKF	8.648	0.083	5.375	1.889	–
	Ours	3.180	0.065	4.186	1.826	70.0
SlopeStair 273.37 m 307.49 s	GaRLILEO	2.359	0.061	2.805	1.051	–
	Leg IEKF	13.382	0.118	20.625	1.203	–
	Vel. IEKF	5.221	0.113	4.339	2.583	–
	Ours	3.058	0.079	4.559	2.046	73.7
Tunnel 247.94 m 277.00 s	GaRLILEO	3.523	0.083	2.849	0.440	–
	Leg IEKF	8.559	0.102	9.761	0.822	–
	Vel. IEKF	5.193	0.081	5.105	1.712	–
	Ours	5.154	0.050	3.961	1.474	70.7
Upstair 197.22 m 227.89 s	GaRLILEO	1.496	0.071	4.048	0.933	–
	Leg IEKF	2.005	0.171	8.068	2.885	–
	Vel. IEKF	2.132	0.151	3.161	2.776	–
	Ours	2.042	0.072	5.037	2.441	71.2
Average	GaRLILEO	2.523	0.075	3.615	0.880	–
	Leg IEKF	11.355	0.270	12.775	1.984	–
	Vel. IEKF	11.551	0.244	4.052	2.362	–
	Ours	2.736	0.070	4.139	2.003	71.3

VII. CONCLUSION AND FUTURE WORK

We proposed a proprioception-only state estimation framework for legged robots that uses a learned measurement model mapping histories of joint-level measurements to body velocity estimates. Under limited data, the error distribution

TABLE IV
RESULTS ON VISION60 DATASET

Sequence	Method	APE _{trans} [m]	RPE _{trans} [m]	APE _{rot} [deg]	RPE _{rot} [deg/m]	$\pi < \gamma$ [%]
2CC2CCW 53.15 m 76.3 s	Leg IEKF	1.344	1.419	1.622	0.280	–
	Vel. IEKF	0.349	1.545	1.953	0.308	–
	Ours	0.278	1.506	1.225	0.299	95.3
2CCW2CC 51.97 m 95.57 s	Leg IEKF	2.095	1.355	0.893	0.290	–
	Vel. IEKF	0.244	1.486	1.483	0.316	–
	Ours	0.226	1.492	1.119	0.315	95.7
3CC3CCW 74.65 m 107.96 s	Leg IEKF	0.756	1.375	0.940	0.282	–
	Vel. IEKF	0.470	1.536	3.137	0.312	–
	Ours	0.667	1.548	3.083	0.312	95.3
3CCW3CC 83.42 m 129.93 s	Leg IEKF	0.901	1.382	0.869	0.287	–
	Vel. IEKF	0.605	1.519	5.216	0.321	–
	Ours	0.363	1.520	1.987	0.315	95.1
RoomScan 38.96 m 66.97 s	Leg IEKF	0.690	1.312	1.140	0.424	–
	Vel. IEKF	0.290	1.444	1.428	0.464	–
	Ours	0.300	1.428	1.356	0.465	95.3
Slipped 19.01 m 43.03 s	Leg IEKF	0.354	1.312	0.707	0.323	–
	Vel. IEKF	0.246	1.499	1.969	0.365	–
	Ours	0.261	1.456	1.044	0.356	95.5
Stroll 99.21 m 162.3 s	Leg IEKF	1.770	1.287	2.427	0.504	–
	Vel. IEKF	0.760	1.505	2.793	0.525	–
	Ours	0.717	1.504	2.912	0.540	94.6
Average	Leg IEKF	1.130	1.349	1.228	0.341	–
	Vel. IEKF	0.424	1.503	2.568	0.373	–
	Ours	0.402	1.493	1.818	0.372	95.26

of these predictions is not Gaussian. We systematically characterize this arbitrary error distribution with a set-coverage statement. This set-coverage statement is then used to update the Gaussian state estimate via KL-divergence and moment matching in a computationally efficient way. We compared our method with a baseline in both simulation and a real-world quadrupedal robot dataset after obtaining calibrated set-coverage statements. Our estimator is competitive with both proprioceptive-only and perception baselines in the nominal Gaussian-noise case and remains consistent and robust in the arbitrary-noise case, whereas baselines do not. Our future work includes extending the proposed legged state estimator with exteroceptive measurements such as vision.

APPENDIX I PROOF OF THEOREM 1

The optimization in (23) is strictly convex in $p(\delta\mathbf{X})$. If $\pi_t \geq \gamma$, the unconstrained minimizer $p_t^* = \bar{p}_t$ (which yields a KL divergence of zero) satisfies all constraints and is therefore uniquely optimal. If $\pi_t < \gamma$, the coverage constraint is active. Introducing dual variables $\lambda > 0$ for the inequality constraint and ν for the normalization constraint, the KKT conditions necessitate that the first variational derivative of the Lagrangian vanishes:

$$\frac{\delta\mathcal{L}}{\delta p(\delta\mathbf{X})} = \ln\left(\frac{p_t^*(\delta\mathbf{X})}{\bar{p}_t(\delta\mathbf{X})}\right) + 1 - \lambda \mathbb{1}_{C_t}(\delta\mathbf{X}) + \nu = 0$$

Solving for $p_t^*(\delta\mathbf{X})$ restricts the optimal solution to the form:

$$p_t^*(\delta\mathbf{X}) = \bar{p}_t(\delta\mathbf{X}) \exp(\lambda \mathbb{1}_{C_t}(\delta\mathbf{X}) - \nu - 1)$$

This indicates $p_t^*(\delta\mathbf{X})$ is a piecewise scaling of the prior: $p_t^*(\delta\mathbf{X}) = k_1 \bar{p}_t(\delta\mathbf{X})$ for $\delta\mathbf{X} \in C_t$, and $p_t^*(\delta\mathbf{X}) = k_2 \bar{p}_t(\delta\mathbf{X})$ for $\delta\mathbf{X} \in C_t^c$. Enforcing the active coverage constraint $\int_{C_t} p_t^*(\delta\mathbf{X}) d\delta\mathbf{X} = \gamma$ using (24) directly yields $k_1 \pi_t = \gamma$. Applying the normalization constraint $\int p_t^*(\delta\mathbf{X}) d\delta\mathbf{X} = 1$ requires the remaining mass to satisfy $k_2(1 - \pi_t) = 1 - \gamma$. Solving for the scaling factors k_1, k_2

recovers (25). The non-negativity constraint is inherently satisfied by the exponential form.

REFERENCES

- [1] I. D. Miller, F. Cladera, A. Cowley, S. S. Shivakumar, E. S. Lee, L. Jarin-Lipschitz, A. Bhat, N. Rodrigues, A. Zhou, A. Cohen, A. Kulkarni, J. Laney, C. J. Taylor, and V. Kumar, "Mine tunnel exploration using multiple quadrupedal robots," *IEEE Robot. Autom. Lett.*, 2020.
- [2] T. Miki, J. Lee, J. Hwangbo, L. Wellhausen, V. Koltun, and M. Hutter, "Learning robust perceptive locomotion for quadrupedal robots in the wild," *Sci. Robot.*, 2022.
- [3] S. Halder, K. Afsari, E. Chiou, R. Patrick, and K. A. Hamed, "Construction inspection & monitoring with quadruped robots in future human-robot teaming: A preliminary study," *J. Build. Eng.*, 2023.
- [4] W. Gong, C. He, K. Su, Q. Li, T. Wu, and Z. Jane Wang, "Didlm: A slam dataset for difficult scenarios featuring infrared, depth cameras, lidar, 4d radar, and others under adverse weather, low light conditions, and rough roads," *IEEE Trans. Intell. Transp. Syst.*, 2026.
- [5] J. Hwangbo, J. Lee, A. Dosovitskiy, D. Bellicoso, V. Tsounis, V. Koltun, and M. Hutter, "Learning agile and dynamic motor skills for legged robots," *Sci. Robot.*, 2019.
- [6] M. Bloesch, M. Hutter, M. Hoepflinger, S. Leutenegger, C. Gehring, C. D. Remy, and R. Siegwart, "State estimation for legged robots - consistent fusion of leg kinematics and IMU," in *Proc. Robot.: Sci. Syst.*, Sydney, Australia, July 2012.
- [7] R. Hartley, M. Ghaffari, R. M. Eustice, and J. W. Grizzle, "Contact-aided invariant extended kalman filtering for robot state estimation," *Int. J. Rob. Res.*, Mar. 2020.
- [8] D. Wisth, M. Camurri, and M. F. Fallon, "Robust legged robot state estimation using factor graph optimization," *IEEE Robot. Autom. Lett.*, 2019.
- [9] C. Noh, S. Jung, H. Kim, Y. Hu, L. Herlant, and A. Kim, "Galileo: Gravity-aligned radar-leg-inertial enhanced odometry," *arXiv*, 2025.
- [10] P. Roth, J. Frey, C. Cadena, and M. Hutter, "Learned perceptive forward dynamics model for safe and platform-aware robotic navigation," *Robot.: Sci. Syst. (RSS 2025)*, 2025.
- [11] A. M. Kulkarni, I. Poulakakis, and G. Huang, "Learning neural observer-predictor models for limb-level sampling-based locomotion planning," 2025.
- [12] R. Buchanan, M. Camurri, F. Dellaert, and M. Fallon, "Learning inertial odometry for dynamic legged robot state estimation," 2021.
- [13] J. Wasserman, A. Agarwal, R. Jangir, G. Chowdhary, D. Pathak, and A. Gupta, "Legolas: Deep leg-inertial odometry," *CoRL*, 2024.
- [14] D. Youm, H. Oh, S. Choi, H. Kim, S. Jeon, and J. Hwangbo, "Legged robot state estimation with invariant extended kalman filter using neural measurement network," in *Proc. IEEE Int. Conf. Robot. Autom. (ICRA)*, 2025.
- [15] S. Lee, H.-B. Kim, and K.-S. Kim, "Legged robot state estimation using invariant neural-augmented kalman filter with a neural compensator," in *Proc. IEEE/RSJ Int. Conf. Intell. Robots Syst. (IROS)*, 2025.
- [16] R. L. Russell and C. Reale, "Multivariate uncertainty in deep learning," *IEEE Trans. Neural Netw. Learn. Syst.*, Dec. 2022.
- [17] N. Tagasovska and D. Lopez-Paz, "Single-model uncertainties for deep learning," *Proc. 33rd Int. Conf. Neural Inf. Process. Syst.*, 2019.
- [18] J. Gawlikowski, C. R. N. Tassi, M. Ali, J. Lee, M. Humt, J. Feng, A. M. Kruspe, R. Triebel, P. Jung, R. Roscher, M. Shahzad, W. Yang, R. Bamler, and X. Zhu, "A survey of uncertainty in deep neural networks," *Artif. Intell. Rev.*, 2021.
- [19] S. Jiménez, M. Jürgens, and W. Waegeman, "Position: Epistemic uncertainty estimation methods are fundamentally incomplete," 2026.
- [20] G. Duran-Martin, M. Altamirano, A. Shestopaloff, L. Sánchez-Betancourt, J. Knoblauch, M. Jones, F.-X. Briol, and K. P. Murphy, "Outlier-robust kalman filtering through generalised Bayes," in *Proc. 41st Int. Conf. Mach. Learn.*, ser. Proc. Mach. Learn. Res., R. Salakhutdinov, Z. Kolter, K. Heller, A. Weller, N. Oliver, J. Scarlett, and F. Berkenkamp, Eds. PMLR, 21–27 Jul 2024.
- [21] C. Combastel, "An extended zonotopic and gaussian kalman filter (ezgkf) merging set-membership and stochastic paradigms: Toward non-linear filtering and fault detection," *Annu. Rev. Control.*, 2016.
- [22] S. Li, T. Stouraitis, M. Gienger, S. Vijayakumar, and J. A. Shah, "Set-based state estimation with probabilistic consistency guarantee under epistemic uncertainty," *IEEE Robot. Autom. Lett.*, 2022.
- [23] S. Wang, "Distributionally robust state estimation for nonlinear systems," *IEEE Trans. Signal Process.*, 2022.

- [24] K. Wang, F. Cuzzolin, K. Shariatmadar, D. Moens, and H. Hallez, "A review of uncertainty representation and quantification in neural networks," *IEEE Trans. Pattern Anal. Mach. Intell.*, 2026.
- [25] R. I. Oliveira, P. Orenstein, T. Ramos, and J. V. Romano, "Split conformal prediction and non-exchangeable data," *J. Mach. Learn. Res.*, 2024.
- [26] V. Mirasierra, M. Mammarella, F. Dabbene, and T. Alamo, "Prediction error quantification through probabilistic scaling," *IEEE Control Syst. Lett.*, 2021.
- [27] G. Casella and R. L. Berger, *Statistical inference*. Duxbury Pacific Grove, CA, 2002.
- [28] G. Shafer and V. Vovk, "A tutorial on conformal prediction," *J. Mach. Learn. Res.*, 2008.
- [29] Y. Sale, A. Javanmardi, and E. Hüllermeier, "Aleatoric and epistemic uncertainty in conformal prediction," in *Proc. 14th Symp. Conformal Probabilistic Predict. Appl.*, ser. Proc. Mach. Learn. Res., K. A. Nguyen, Z. Luo, H. Papadopoulos, T. Lofström, L. Carlsson, and H. Boström, Eds. PMLR, 10–12 Sep 2025.
- [30] J. Shore and R. Johnson, "Properties of cross-entropy minimization," *IEEE Trans. Inf. Theory*, 1981.
- [31] K. Ganchev, B. Taskar, and J. Gama, "Expectation maximization and posterior constraints," *Adv. Neural Inf. Process. Syst.*, 2007.
- [32] A. Genz and G. Trinh, "Numerical computation of multivariate normal probabilities using bivariate conditioning," in *Springer Proc. Math. Stat.*, ser. Springer Proc. Math. Stat. Cham: Springer International Publishing, 2016.
- [33] D. J. McDonald, C. R. Shalizi, and M. Schervish, "Estimating beta-mixing coefficients via histograms," *Electron. J. Stat.*, 2015.